

Advanced Data Transfer Strategies for Overset Computational Methods

Eliot W. Quon* and Marilyn J. Smith†

School of Aerospace Engineering, Georgia Institute of Technology, Atlanta, GA

A data transfer strategy applicable to overset simulations has been developed with scattered data interpolation techniques. This approach applies a “cloud”-based radial basis function algorithm in lieu of traditional trilinear mappings and the resulting data transfer has no dependence on grid connectivity. Therefore it is ideally suited for the resolution of general grid configurations and eliminates problems associated with orphan points. The effectiveness of the data transfer methodology has also been demonstrated for application with hybrid approaches involving multiple solvers operating on overlapping computational domains. A diverse set of applications have been considered including a convecting vortex, a turbulent ship airwake, and a wind turbine rotor in axial flow.

Nomenclature

α	Radial basis interpolation coefficient
β	Polynomial interpolation coefficient
Δs	Isotropic grid spacing
Δt	Simulation time step size
Φ	Radial basis kernel, $\Phi(\vec{x}, \vec{x}_i) = \phi(\ \vec{x} - \vec{x}_i\ _2)$
ϕ	Radial basis function (RBF), $\phi(r)$
ρ_∞	Free-stream density
N	Number of interpolation donor points
p	Pressure
Q	Number of polynomial coefficients
r	Radial (Euclidean) distance, $\ \vec{x}\ $
s	Interpolant to an unknown function
u	x -component of velocity
U_∞	Free-stream velocity magnitude
v	y -component of velocity
X	Set of donor points
$()^T$	Matrix transpose

I. Introduction

Within the aerospace community, many applications of interest require the prediction of the unsteady aerodynamics of both lifting and bluff bodies moving in multiple frames of reference. State-of-the-art computational fluid dynamics (CFD) requires an efficient means of handling the evolution of computational domains with mesh motion, deformation, and/or grid adaptation. The Chimera overset method^{1,2} grew out of this need for a general approach to efficiently model complex flows by combining solutions on composite overlapping meshes. Each moving component is modeled by structured or unstructured body-fitted grids that are overset onto one or more stationary background grids that model the remainder of the flow field.

*Ph.D. Candidate, AIAA Student Member

†Professor, AIAA Associate Fellow

Additional solution steps include hole cutting to remove points outside the computational domain (i.e., interior to solid boundaries) and interpolation to transfer the flow solution at non-coincident points between overlapping meshes. This approach has been readily applied to the analysis of moving grid systems including rotorcraft, wind turbines, and store separation.³⁻⁵

The data transfer aspect of the overset solution entails calculating the solution at target locations known as *receptors* based on the solution from source points known as *donors*. These donors may generally come from one or more grids and are identified by a search procedure typically performed within additional software. After donors are found, a general approach to obtaining the solution at receptors relies on isoparametric mappings with trilinear basis functions. These are calculated with Newton's method and are applicable to both structured and unstructured grids.^{6,7} On a Cartesian or structured mesh, trilinear interpolants may be directly evaluated because the computational and parametric spaces are topologically identical. This approach requires a set of acceptable donor points to form an interpolation stencil which cannot always be found. For instance, when adjacent grids have insufficient overlap or if significant disparities in mesh spacing between grid levels exist, complete stencils of donor points cannot be formed and the associated receptors become known as "orphan" points. As a result, solution fidelity may be compromised because the solution at two levels of fringe points cannot be resolved to maintain high-order accuracy.⁸ To permit the solver to continue, solutions at orphan locations are typically estimated by an averaging procedure.^{5,9,10} The problem of orphan points is exacerbated by relative mesh motion which can increase the number of orphans and/or change their locations over time.

Two general mitigation approaches exist when orphan points are present. First, the grids may be re-designed to improve the quality of mesh intersections. However, straightforward adjustments are not always possible, especially when considering complex geometries, and grid refinement can significantly increase cost. For example, a wing-store configuration studied by Power et al.⁵ had 0.5% of all cells orphaned; application of an adaptive mesh refinement procedure eliminated all orphans with an increase in total cell count of 10%. Alternatively, a dense interface grid may be added in the orphan region.^{5,11} These approaches require user intervention and added cost, either in engineering hours or computational time.

As an alternative, cloud-based data techniques can provide a mapping between arbitrarily structured data samples and are decoupled from solver type (e.g., unsteady Reynolds-averaged Navier-Stokes, vorticity-velocity, or potential flow methodologies) and topology (Cartesian, structured, and unstructured). While these approaches are well-established within other fields (e.g., computer graphics, digital elevation modeling, or optical design) their application to CFD problems has been limited. Recommendations from a number of authors have suggested that scattered data interpolation with radial basis functions (RBFs) is a general, accurate approach¹²⁻¹⁴ and can also eliminate numerical errors due to orphan points in overset simulations. Since donor points can be sourced from any location on any grid, the approach naturally precludes scenarios involving a lack of sufficient donor points. These methods are especially attractive for overset data transfer because:

1. They permit interpolation and extrapolation¹⁵ based on arbitrarily clustered clouds of points in any dimensional space.
2. They have in general higher-order accuracy that can be increased by freely adding data points.
3. They are directly applicable to unstructured methodologies since the interpolant is decoupled from the computational mesh, eliminating requirements on the spatial structure of the sampled data.
4. They can be readily applied to the problem of solution transfer in overset methods since they do not require connectivity information.

In the same way that cloud-based techniques are applicable to overset methods, hybrid methods can also benefit from improvements in data transfer. Hybrid approaches feature overlapping or non-contiguous computational domains, with the primary difference being that the domains are resolved by different methodologies. The chosen solvers may emphasize different physics and operate with potentially different spatial and temporal requirements. To obtain a coupled solution, solutions must be exchanged periodically between solvers, typically at every iteration. Using this approach, substantial improvements in terms of both spatial accuracy and solver efficiency have been recently achieved for a variety of flows including lifting and bluff bodies.¹⁶⁻¹⁸

II. Numerical Approach

A radial basis function (RBF) is a univariate function of Euclidean distance from a chosen *center* \mathbf{x}_c :

$$\Phi(\mathbf{x}, \mathbf{x}_c) = \phi(\|\mathbf{x} - \mathbf{x}_c\|_2) = \phi(r). \quad (1)$$

An RBF interpolant based on a set of donor points X has the following form:

$$s_{f,X}(x) = \sum_{j=1}^N \alpha_j \Phi(x, x_j) + \sum_{k=1}^Q \beta_k p_k(x), \quad (2)$$

where s is the RBF interpolant of the function f evaluated at an arbitrary location x ; α_j and β_j are the interpolation coefficients to be determined; and x_j are the RBF centers that coincide with the set of sampled data X . p_k is chosen to be a polynomial basis to ensure a unique solution to the interpolation problem.¹⁹ An additional constraint is placed on the function p_k to ensure solvability of the interpolation system:¹⁴

$$\sum_{j=1}^N \alpha_j p_k(x_j) = 0. \quad (3)$$

Equations 2 and 3 are combined and solved as a linear system of equations:

$$\begin{bmatrix} A_{\Phi,X} & P \\ P^T & 0 \end{bmatrix} \begin{Bmatrix} \alpha \\ \beta \end{Bmatrix} = \begin{Bmatrix} f \\ 0 \end{Bmatrix}, \quad (4)$$

where the submatrices are defined as:

$$A_{\Phi,X} = (\Phi(x_j - x_k)) \in \mathbb{R}^{N \times N} \quad (5)$$

$$P = (p_k(x_j)) \in \mathbb{R}^{N \times Q}. \quad (6)$$

Solution of Eqn. 4 produces an interpolant that depends on both spatial coordinates and the local solution field.

II.A. Data Transfer

The data transfer algorithms considered in the present work focus on two basis functions which are accurate and robust. The thin-plate spline (TPS) function has been recommended for both interpolation and extrapolation:²⁰

$$\phi(r) = r^2 \log(r), \quad (7)$$

and the compactly-supported Wendland C^2 (W2) basis function has been recommended in Refs. 21–23:

$$\phi(r) = \begin{cases} (1-r)^4(4r+1), & r \leq 1 \\ 0, & r > 1. \end{cases} \quad (8)$$

These functions are free from additional problem-dependent shape parameters, thus facilitating the implementation of these algorithms for a variety of applications. The derivation of the W2 function ensures continuity up to the second derivative (i.e., it is C^2 smooth).¹⁴ Since most CFD meshes have high levels of resolution, the increased smoothness of higher-order functions within the Wendland C^k family of functions (with $k > 2$) provides no added benefit²⁴ and therefore is not presented. The prior efforts with these functions have focused on applicability to non-coincident fluid-structure interfaces rather than applicability to general data type interpolations. Costin and Allen²³ applied the Wendland function only to interpolation across non-matching Cartesian grid interfaces rather than unstructured overlapping grids.

When applying a compactly-supported RBF such as the Wendland C^2 function, the region of influence for a particular data point is dictated by a support radius that scales the independent variable. In Eqn. 8, the radius r is normalized by the support radius so that the function is identically zero outside of the supported region. Larger support radii will result in a smoother interpolated field,²⁵ indicating that for fluid dynamic

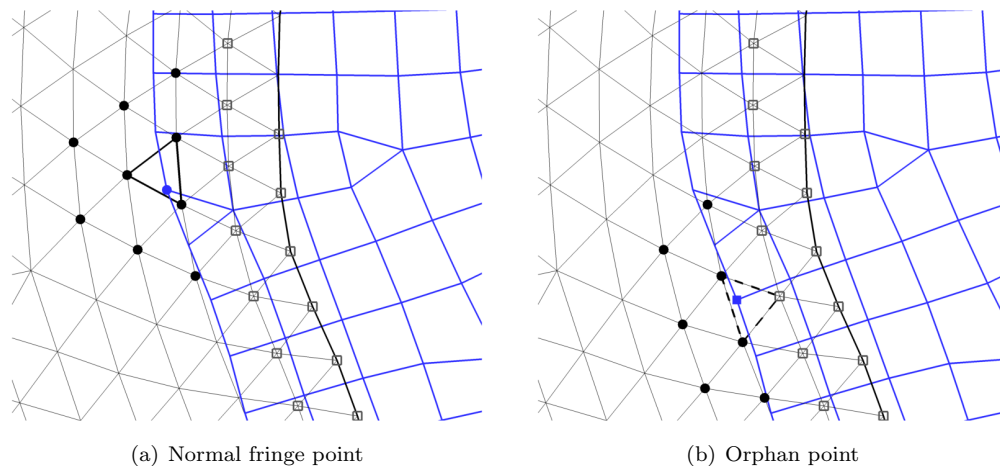


Figure 1. Clouds of source points in the vicinity of orphan points. Filled black circles denote donors while square symbols indicate orphans. The cell enclosing the receptor point is outlined on the black grid.

applications the choice of support radius is problem and grid dependent. Therefore a constant value for the support radius was not explicitly specified *a priori* as commonly applied in literature^{23,26} but rather was permitted to vary depending on the local mesh density as described by Ref. 27. This is accomplished by translating and scaling the coordinates of the donor points so that the points enclosing the receptor lie within a unit domain centered at zero.

Clouds of interpolation points are formed by first identifying the cell enclosing the receptor point or the donor closest to the receptor if an enclosing cell cannot be located (in the case of orphan fringe points). Using the cell nodes (or single donor) as the starting location, the set of donor points is formed by including neighboring nodes. The cloud should include at minimum all nearest neighbors to the receptors point, e.g., the nodes of the enclosing computational cell.²⁶ In practice however, this offered no appreciable improvement over linear interpolation approaches,²⁸ therefore an additional level of points from neighbors of these nodes was also included in the cloud. To maintain feasibility in terms of computational cost, expanding the neighborhood of points beyond a single level of surrounding nodes has not been considered. Some sample clouds of donor points are illustrated in Fig. 1.

II.B. Treatment of Orphan Points

When applying a cloud-based interpolation method, the same approach to data transfer may be applied to configurations both with and without orphan points. Since there is no requirement that the receptor point be located within a particular cell (as with standard mapping techniques) or that the donor points are connected (to form a stencil as required for polynomial-based techniques), points may be arbitrarily included in the data transfer to compensate for a lack of resolution in the immediate vicinity of the receptor. In the current implementation, donor points that are also fringe points are automatically removed from the interpolation cloud. The size of the cloud is allowed to vary in size to accommodate receptor points with insufficient donors. If the number of non-fringe donors is less than or equal to the number of points comprising a single cell (a minimum requirement to maintain linear interpolation resolution²⁸), additional donors are sourced from neighbors of nodes already in the cloud until the minimum donor requirement is met. The selected cloud of source points does not necessarily encompass the target point when considering orphans, thus requiring extrapolation. However, the RBF data transfer algorithm applied to both interpolation and extrapolation is identical and invisible to the user.

III. Computational Tools

The baseline numerical analysis that was selected for overset development is FUN3D,²⁹ a fully unstructured, unsteady Reynolds-Averaged Navier-Stokes (URANS) solver developed primarily at NASA Langley Research Center. Numerical schemes implemented in the code are spatially second-order accurate with Roe upwinding and temporally second-order accurate using multi-step backward difference formulas. FUN3D includes overset

mesh capabilities for accurate resolution of complex geometries and multiple frames of motion, for example in rotorcraft applications.³⁰

Two auxiliary codes are included to provide overset capabilities to FUN3D: **Suggar++** (Structured, Unstructured Generalized overset Grid Assembler) and **DiRTlib** (Donor Interpolation Receptor Transaction library).^{9,31} **Suggar++** handles grid transformations and hole-cutting, donor-receptor identification, and calculation of interpolation weights. **DiRTlib** interfaces with the flow solver and uses the domain connectivity information generated by **Suggar++** to calculate interpolated values. For static meshes, **Suggar++** performs as a preprocessor to match donor points with receptor points, after which interpolation weights are calculated based on donor locations only. For dynamic meshes, **Suggar++** is both a preprocessor and an iterative routine operating within FUN3D. At each solver time step and subiteration (for time-accurate simulations), **DiRTlib** retrieves the solution at donor points and updates the solution at fringe points. To provide a cloud of source points for the scattered data technique, the standard donor search procedure has been modified to return not only the cell nodes encompassing the receptor node, but the neighbors of these cell nodes as well. Connectivity information is not required for the scattered data interpolation but has been utilized for convenience to avoid nearest neighbor searches. The interpolation matrices are calculated prior to flow solution, and matrix inversion takes place either as a preprocessing step for static meshes or on the fly for dynamic meshes. The resulting data transfer depends on both donor locations and the local solution field.

For the hybrid simulations in the present work, the far field wake analysis is provided by VorTran-M,³² a three-dimensional volumetric wake solver developed by Continuum Dynamics, Inc. (CDI). VorTran-M performs a direct numerical solution of the unsteady incompressible Navier-Stokes equations in vorticity-velocity form. Velocities are computed at each step using a Cartesian fast multipole method. A discretization of the governing equations is obtained by Toro's Weighted Average Flux (WAF) algorithm and Strang spatial splitting which explicitly conserves vorticity. The effects of numerical diffusion are controlled by the WAF flux limiter. Solid bodies are not directly modeled but can be represented through solution coupling to a near-body solver. The formulation has demonstrated high-resolution rotor wake predictions on low-cell count grids when coupled to a variety of near-body solvers (Euler/RANS, structured/unstructured, octree Cartesian, and overset) for a number of vorticity-dominated flows.^{33,34}

IV. Evaluation Cases

Three different test cases have been considered in the present work. The first is the overset simulation of an inviscid convecting vortex, a standard feature of many fluid dynamics problems. The second test case is the overset calculation of a three-dimensional, turbulent ship airwake. Finally, a hybrid calculation of a wind turbine rotor has been performed.

IV.A. Inviscid Convecting Vortex

A vortical disturbance was written in a form consistent with the non-dimensionalization scheme in FUN3D.³⁵

$$\frac{u}{U_\infty} = 1 - \frac{C}{U_\infty R} \frac{y - y_c}{R} \exp\left(\frac{-r^2}{2}\right) \quad (9)$$

$$\frac{v}{U_\infty} = \frac{C}{U_\infty R} \frac{x - x_c}{R} \exp\left(\frac{-r^2}{2}\right) \quad (10)$$

$$\frac{p - p_{norm}}{\rho_\infty U_\infty^2} = 1 - \frac{C^2}{2U_\infty^2 R^2} \exp(-r^2) \quad (11)$$

$$r^2 = \frac{(x - x_c)^2 + (y - y_c)^2}{R^2} \quad (12)$$

with a constant density $\rho = \rho_\infty$, free-stream velocity U_∞ , and $p_{norm} = p_\infty - \rho_\infty U_\infty^2$. The vortex is centered at (x_c, z_c) with a nominal core radius R of 1.0 and non-dimensional vortex strength $C/U_\infty R$ of 0.02.

Overset simulations dependent upon linear interpolation perform data transfers with only the nodes of the cell enclosing the target point. For this two-dimensional configuration, computational cells are triangles and quadrilaterals that have been extruded to form volumes for the three-dimensional flow solver. Therefore trilinear interpolation functions are applied in the standard overset implementation. For this linear approach, the number of donor points is fixed by the element type of the donor cell regardless of the presence of orphan

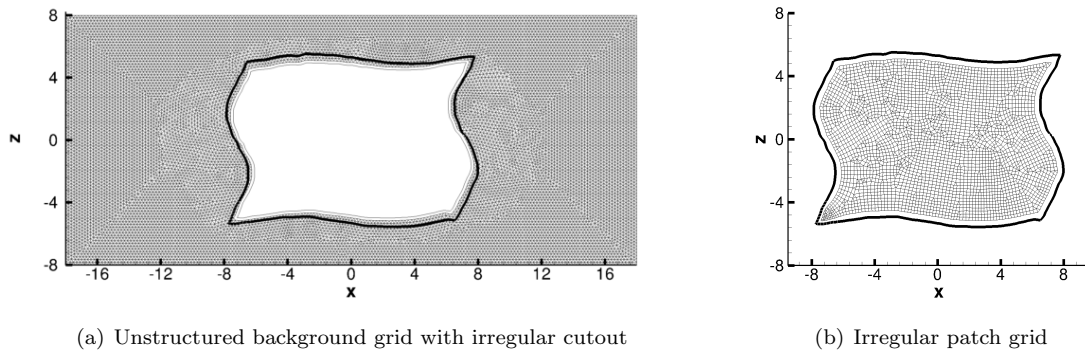


Figure 2. Overset grid systems for advanced overset investigations with orphan points ($\Delta s = 0.2$); outlined region denotes the extent of the patch grid.

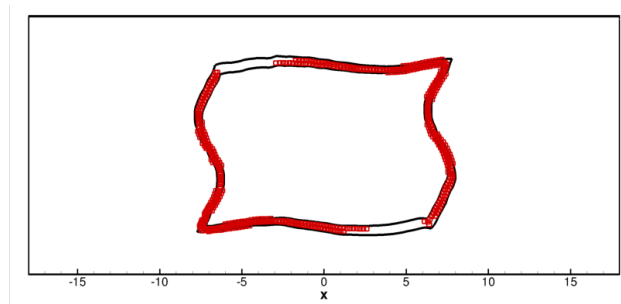


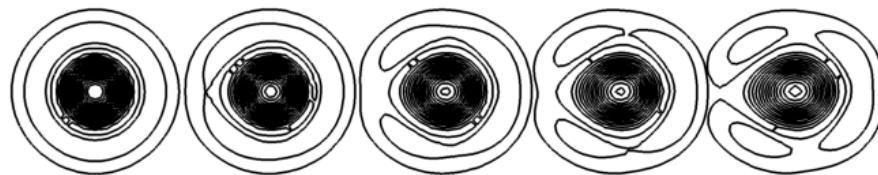
Figure 3. Sample modified overset grid configuration with orphan points shown as red square symbols.

points. In comparison, the cloud-based RBF interpolations are based upon a neighborhood of typically 23–24 nodes on average, nearly a four-fold increase. This indicates that most triangles are connected to nine other nodes on average (numbering 12 nodes on a two-dimensional plane). In the presence of orphan points in the configurations tested, the number of available donors decreases by 19–38% in this configuration. To increase accuracy over linear interpolation, the point selection algorithm required that the number of donor points in the cloud not be less than the number of nodes comprising a single cell. In this case, the minimum allowable number of donors was six but the actual minimum number of points per cloud was ten.

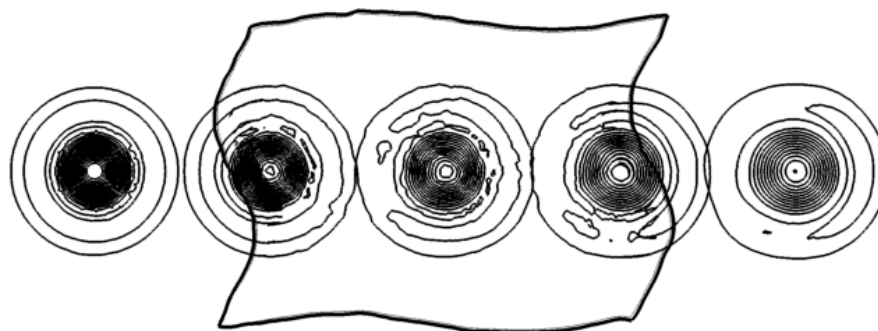
Unstructured overset grid configurations with and without orphan points were created from the meshes depicted in Fig. 2. For this evaluation, the mesh spacing was chosen to provide ten computational cells across the vortex core. A configuration with orphan points were created by resizing the background grid to have an approximately 20% larger cutout region. This reduces the size of the overlap region and transforms over half of the fringe points into orphans due to the poor quality of donors. These are illustrated by the symbols in Fig. 3. Since these orphan points cannot be adequately resolved under the original overset interpolation paradigm, an effective gap in the computational grid is formed.

The vortex solution was initialized on the background grid (Fig. 2(a)) and advanced until the vortex convected once through the patch grid (Fig. 2(b)), ending downstream on the background grid. Non-periodic far-field boundary conditions were applied. At each time step, subiterations were performed until temporal errors decreased by an order of magnitude. Calculations on both single and overset grid configurations resulted in the flow fields illustrated by Fig. 4. The orphan-free overset solution preserves the same qualitative features as the single-grid case, which exhibits minor dissipation due to the coarseness of the mesh (Figs. 4(a) and 4(b)). If orphan points are present, linear interpolation includes averaging at the overset gap which dissipates the vortex structure after passage through the second overset boundary (Fig. 4(c)). In comparison, the cloud-based data transfer approach utilizing TPS or W2 interpolation (Fig. 4(d)) eliminates the uncertainty at orphan locations arising from any averaging procedure. The RBF algorithm systematically includes additional donors in the interpolation so that the local solution is adequately reproduced (Fig. 4(d)). The W2 solution field has not been shown as it is visually indistinguishable from the TPS solution.

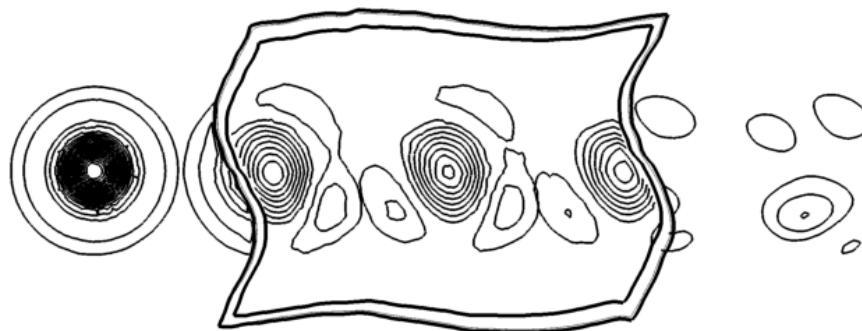
Conservation errors were calculated from instantaneous solutions for the trilinear and RBF interpolation methods. The extent to which the conservation laws of fluid dynamics are satisfied were considered by evaluating the net mass and momentum fluxes in and out of the computational domain; any deviation from



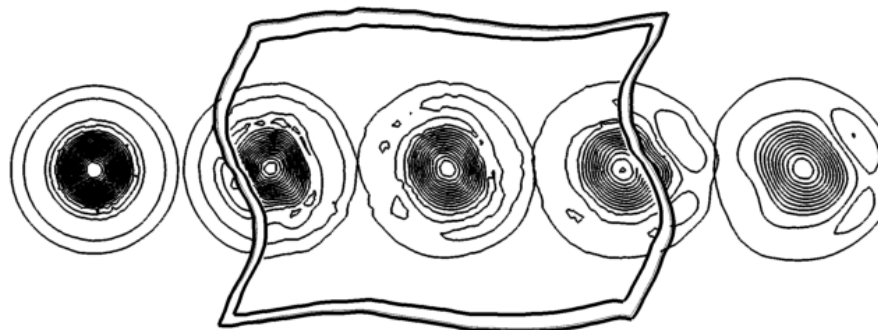
(a) Single Grid



(b) Overset, no orphans



(c) Overset, with orphans and linear mapping



(d) Overset, with orphans and advanced mapping

Figure 4. A comparison of the vorticity field for a single-grid case, an overset case without orphans, and two overset cases with orphans. Five solution snapshots have been super-imposed on top of each other.

zero is considered conservation error. Romberg integration was applied to estimate the numerical fluxes in the limit of zero grid spacing. For $N = 2^k + 1$ equally spaced points where k is a positive integer, the algorithm performs k iterations to remove error terms up to (but not including) $\mathcal{O}(1/N^{2k})$.³⁶ To initiate this procedure, the boundary solutions were collocated to provide a number of equally spaced points equal to $2^k + 1$. The shortest integration path (with the fewest points and thus the highest theoretical error) was at the upstream and downstream boundaries. On the evaluation mesh, these boundaries contained 81 points which were interpolated to 129 locations (for $k = 7$), resulting in an integration error on the order of $s\mathcal{O}(\Delta s^{2k}) \approx 10^{-10}$ or lower.

The mass fluxes in and out of the computational domain were calculated with the Romberg technique. The exact massflow has a non-dimensional value of 16.0, while the difference between the massflow leaving and entering the computational domain is on the order of 10^{-7} or lower for all configuration without orphan points (Table 1). Positive or negative values indicate that mass has been added or removed, respectively, during transit through the overset grid system. The columns in Table 1 indicate the conservation error at the beginning, middle, and end of the simulation when the vortex is located on the background or patch grids in Fig. 2. When orphan points are present, error in massflow is initially an order of magnitude lower when the data transfer is performed with a cloud-based approach. Moreover, the RBF interpolation maintains the same level of massflow error while trilinear interpolation errors increase by two orders of magnitude over the course of the calculation.

Table 1. Net mass flux through the computational domain when the convecting vortex is at different locations in the overset grid configuration.

	Orphans	Initial Bkg.	Patch	Final Bkg.
Trilinear Interpolation		1.36×10^{-8}	-4.85×10^{-7}	-1.21×10^{-8}
Thin-plate spline		-1.34×10^{-9}	-4.16×10^{-7}	7.87×10^{-7}
Wendland C^2		-9.87×10^{-9}	1.98×10^{-8}	-3.82×10^{-7}
Trilinear Interpolation	x	-1.10×10^{-5}	6.39×10^{-6}	-7.49×10^{-4}
Thin-plate spline	x	2.59×10^{-6}	-1.36×10^{-6}	-4.07×10^{-6}
Wendland C^2	x	2.50×10^{-6}	-1.27×10^{-6}	-3.75×10^{-6}

The conservation errors in mass, x -momentum, and z -momentum on the orphan configuration are plotted for the duration of the simulation in Fig. 5. For all three quantities, the error on the single grid is of the order 10^{-7} , which is greater than the error in the numerical integration and therefore significant. Errors are introduced in the overset simulations when the vortex is in the vicinity of the overset interfaces at $x \approx -6$ and $x \approx 6$. These errors appear as local maxima in the computed net flux, with double peaks appearing prominently at $x \approx -9, -5, 6,$ and 9 in Figs. 5(a) and (c). These peaks correspond to the passage of the front and rear of the vortex core where swirl velocity and velocity gradients are at a maximum.

The mass conservation error returns to the approximate unperturbed level at $x \approx -4$ after the vortex core has crossed from the background onto the overset patch grid. The vortex exiting the patch to the background grid through the second set of fringe points (beginning at $x \approx 4$) has consistently higher error

Table 2. Cost in terms of averaged wallclock time per step for the convecting vortex evaluation case.

Case	Method	Fringes	Avg Subiters.	Cost / step [s]
Baseline overset configuration	Trilinear	1,894	8.87	2.1718
	TPS	1,894	9.02	2.3416
	W2	1,894	9.02	2.2868
Overset configuration with orphans	Trilinear	884	36.2	4.6648
	TPS	2,036	37.1	5.2125
	W2	2,036	36.0	5.1956

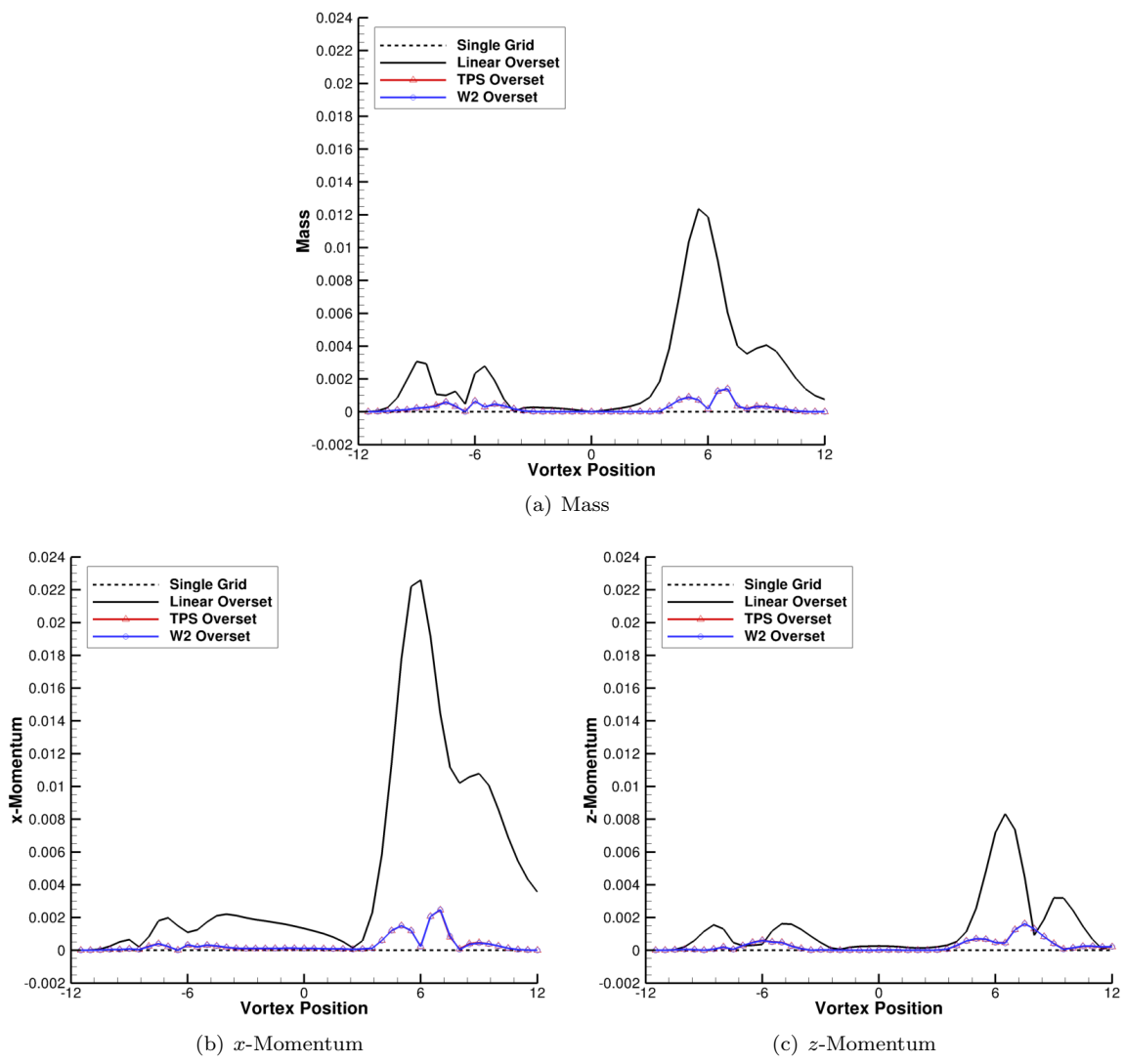


Figure 5. Calculated net flux through the outer boundary of the computational domain for the inviscid convecting vortex test case.

than the passage through the first set of fringe points. While the fluxes in both the linear and advanced overset simulations display the same trends over time (or as a function of vortex position), applying an RBF interpolation technique does not simply scale the errors. For instance, the large increase in conservation error is accompanied by a delayed return to the unperturbed level in all three quantities, most notably in the streamwise momentum (Fig. 5(b)). In addition, the mass and x -momentum fluxes have not returned to initial levels even at the end of the simulation (Figs. 5(a) and (b)).

The cost of simulating each of the vortex cases on a single processor is summarized in Table 2. For the cases without orphans, the cost increase associated with applying RBF interpolation was negligible, on the order of 0.1 seconds of wallclock time per iteration. With orphan points in the grid configuration, the linear overset approach applies an averaging procedure whereas the RBF approach interpolates all fringe points in the same manner thus adding cost. However, the increase in cost primarily stems from the increase in the number of subiterations required to attain temporal convergence.

IV.B. Ship Airwake

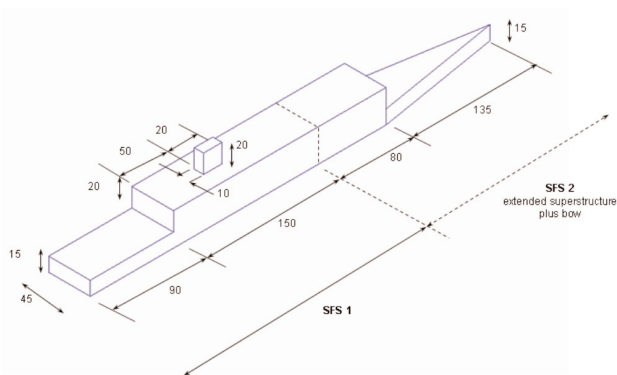


Figure 6. Geometries for the SFS and SFS2 configurations with dimensions in feet, from Ref. 37.

Maritime air vehicles operating from or near naval vessels typically encounter complex vortical structures shed from the bow and other ship structures such as hangars, decks, turrets, cables, and parked air vehicles. A helicopter trying to land on a ship deck aft of a hangar may have to descend through a shear layer emanating from the roof of the hangar or interact with a region of recirculating flow in the hangar wake. An international collaborative effort³⁸ has led to the development of a generic ship model known as the “simple frigate shape” (SFS) which has been extensively studied. A later iteration of this generic model developed by the Technical Co-operation Programme to allow standardized study of ship topside aerodynamics³⁷ is known as the “simple frigate shape 2” (SFS2). The SFS2 introduced a more realistic, streamlined bow geometry (Fig. 6) and has since superseded the SFS. New wind tunnel results of the SFS2 configuration have been obtained by the U.S. Navy from the Naval Surface Warfare Center Carderock Division (NSWCCD) and are available for additional validation. Recent efforts have studied a full-scale SFS2 in free air in addition to a 50th-scale model in the NSWCCD test section.³⁹ The current work utilizes the same computational grids and simulates 70.6 ft/s headwind conditions at a computational time step equal to 0.0005 s per step, corresponding to the experimental sampling rate. The overset approach permits simulation of these conditions using identical or similar grids as the previous single-grid simulations that modeled a ship in the NSWCCD test section. After creating a background grid and a near-ship grid, a variety of operating conditions (e.g., at different headings and/or with ship motion) may be simulated without the need to generate additional computational grids, thus facilitating a parametric analysis. The ship is modeled with viscous surfaces and the far field is modeled with a Riemann invariant condition. The sea boundary is considered to be part of the far field, neglecting the moving interface between the air and water.

Free-air grids were created from an existing grid which modeled the SFS2 in the NSWCCD wind tunnel test section³⁹ with point clustering on the viscous floor, ceiling, and side walls removed. Since a URANS simulation is able to provide large quantities of flow-field data not available from experiment, a single grid configuration was created for reference as a best possible solution to compare with the overset solutions. The free-air overset configuration includes a rectangular background grid extending outward 4.5 ship lengths in the streamwise and lateral directions, and extending 0.75 ship lengths normal to the sea plane. The ship

surface point distribution was kept identical in the single and overset grid configurations to maintain grid quality ($y^+ < 1$) and permit comparisons between grids. The specified far-field mesh spacings were also kept the same. The single grid contained 2.7 million nodes and the overset configuration added 54,958 fringe nodes at which interpolations are performed.

The flow field was sampled and averaged over the period of time required for the flow to traverse a distance of one ship length. Figure 7 depicts averaged flow fields for the linear and RBF overset approaches. For all calculations, the flow above the forward deck is identical. Differences in the flow are visible above the rear deck near and above the height of the hangar. The ship features have been annotated on the single grid solution (Fig. 7a), and bold contour lines in Fig. 7 indicate streamwise velocities between $0.7-0.8V_\infty$. These contours bracket the region with the most significant differences between linear and RBF overset calculations. For comparison between the single and overset grid configurations, all solutions were collocated onto an identical Cartesian mesh. In comparison with the single grid solution, average streamwise velocity errors were 7% lower when applying thin-plate splines or Wendland C^2 interpolation rather than trilinear interpolation. Average normal velocity errors were 15% lower with TPS rather than trilinear interpolations and 35% lower when interpolating with the W2 basis. Application of an RBF approach also reduced the maximum error in both velocity components by 17–43%.

A flow recirculation region behind the hangar was observed in the original SFS experiment⁴⁰ and is characteristic of flows over a backward-facing step. The reversed flow above the aft flight deck (Fig. 7) exhibits this behavior as expected. Flow conditions for this evaluation case correspond to a Reynolds number based on hangar height of 1.82×10^5 . High Reynolds number experimental data in the literature are in the 5×10^3 to 4×10^4 range.⁴¹ Therefore the single grid and overset simulations have not been compared to experiment. To estimate the locations at which the unsteady flow separates and reattaches on the flight deck, skin friction contours were extracted from the ship surface. Contour lines at which the skin friction was equal to zero were identified. The locations along the ship centerline where separation occurs have been tabulated in Table 3, along with reattachment locations.

Table 3. Locations of separation and reattachment on the ship deck, normalized by hangar height.

Overset Method	Separation Location	Reattachment Location
Single Grid	0.5247	2.5646
Trilinear Interpolation	0.4763	2.6212
Thin-plate spline	0.5175	2.6099
Wendland C^2	0.5171	2.6271

Under current flow conditions, the recirculation region spans over half the length of the flight deck. The flow separates from the deck at a distance of approximately half the hangar height (h) and reattaches at approximately $2.6h$ along the deck. The separation location calculated from the overset simulation with trilinear interpolation differs from the single grid solution by 9%. In comparison, both RBF overset interpolation methods predict a separation location within 2% of the single grid solution. In terms of reattachment location, estimates with linear and cloud-based overset methods all differ from the single grid solution by approximately 2%.

The ship airwake case was run in parallel on 256 processors. When applying RBF interpolation, the average size of the interpolation problem based on the number of average donors increases eightfold from 8 to 32. In three dimensions, the number of donors is approximately 30% higher than the two-dimensional vortex case, resulting in increased cost. However, parallel solver operation reduces the number of fringe points per processor and as a result the added interpolation time is only 6% of the total solver cost per step (Table 4).

IV.C. Wind Turbine Rotor

Forecasts predict that wind energy will meet roughly 20% of the United States national energy demand by the year 2030.⁴² In order to harness the estimated 8,000 gigawatts of available wind resources, key technological improvements improving both on- and off-shore power production must be realized including larger rotors and advanced blade designs. These and other engineering advancements summarized in Ref. 42 motivate larger, more sophisticated analyses. In addition, unsteady interactions with the vortical rotor wake

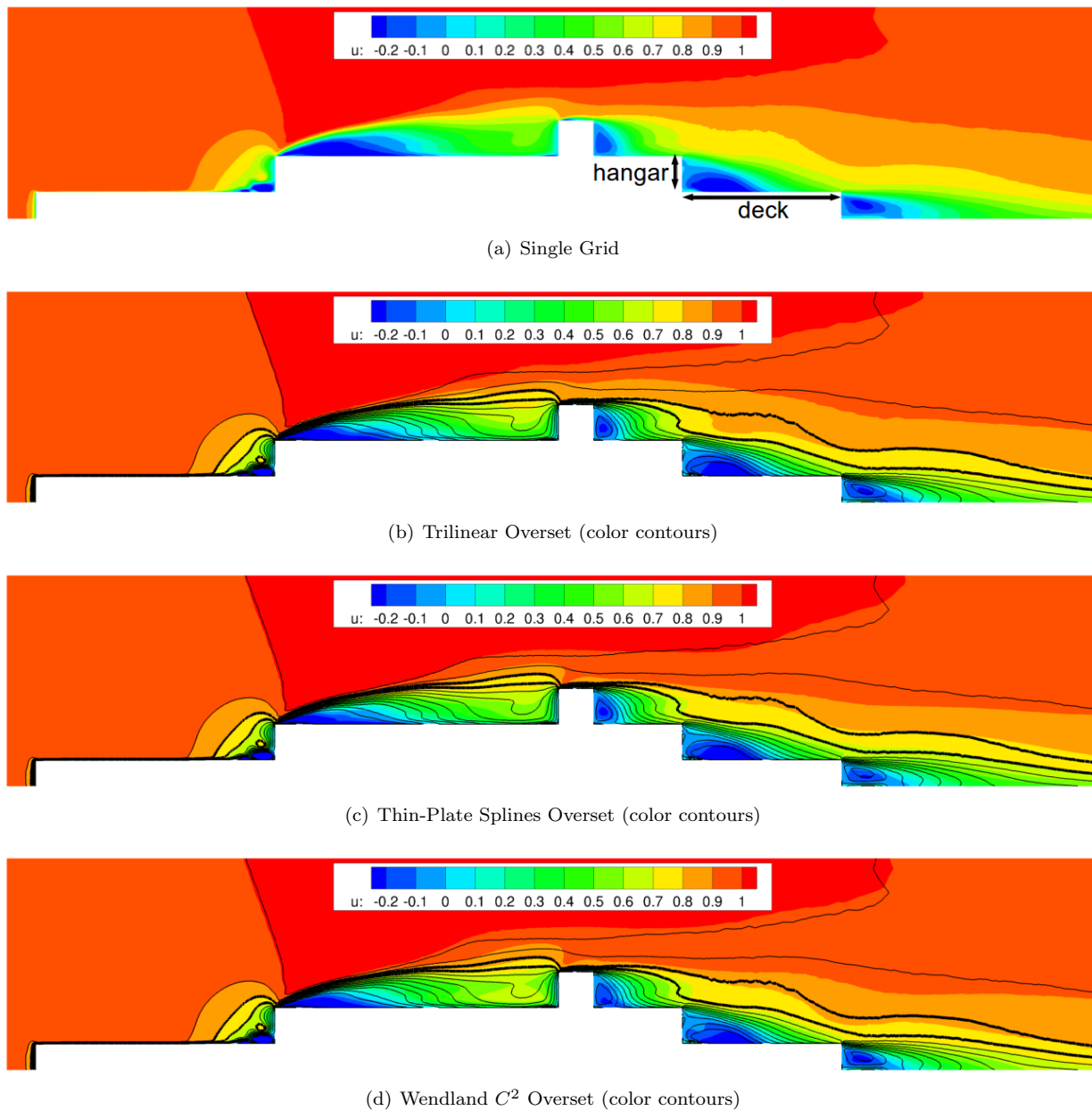


Figure 7. Averaged contours of streamwise velocity for single and overset grid configurations, viewed from the port side. In the overset cases, black line contours represent the single grid solution.

Table 4. Cost in terms of averaged wallclock time per step for the ship airwake evaluation case.

Overset Method	Average cost/step [s]
Trilinear interpolation	18.8474
Thin-plate spline	19.9706
Wendland C^2	20.0179

cause undesirable noise and fatigue loading⁴³ and can be challenging to accurately capture. The preservation of all relevant flow features requires high cell-count grids to avoid numerical dissipation. Therefore, cost-effective hybrid methods can offer an attractive alternative to traditional URANS calculations. In the current hybrid approach, the near-body URANS solution performed by FUN3D is coupled to a vorticity-velocity (V-V) analysis in the far field, VorTran-M. This eliminates the need to model the entirety of the flow field with URANS. The near-body domain is overset onto an adaptive Cartesian background mesh, and overset hole-cutting is replaced by a direct blanking procedure.⁴⁴

For a fully-coupled solution between the near-body and wake solver, velocities are transferred from the near-body mesh onto the background mesh at each solver iteration. These velocities determine the vorticity within near-body cells on the background mesh, and the wake solution is advanced with the updated solution from the near-body solver. After the wake solution is updated, the induced velocities from the entire vorticity field modify the Riemann invariants on the URANS near-body boundary.²⁸ While a continuous velocity field can be recovered from the wake by the Biot-Savart law,³³ transfer of the near-body solution to the wake requires overset interpolation. As a demonstration of how the application of a cloud-based interpolation strategy can increase simulation accuracy, the thin-plate splines and Wendland C^2 radial basis functions compared with trilinear interpolation.

A popular evaluation case within the wind energy community is the Unsteady Aerodynamics Experiment (UAE) conducted by the National Renewable Energy Laboratory (NREL). The UAE Phase VI studied a 10 m, 20 kW wind turbine in the 80 by 120-foot wind tunnel at NASA Ames.⁴⁵ This experiment demonstrated a range of three-dimensional unsteady aerodynamic phenomena and has provided ample test data for the international research community. In the current work, an isolated rotor at 0° yaw in a 15 m/s free stream was evaluated on a reduced grid. An efficient analysis modeling a single rotor blade with rotational symmetry was performed with the hybrid methodology. This approach provided a 70% reduction in the number of computational nodes compared to overset simulations of a full upwind turbine.⁴ A time step size of 0.5° azimuth per step was applied with a temporal error tolerance of 5%, as recommended in prior work.^{4,18} The baseline blade computational mesh included 4.5 million nodes (17.7 cells). The cost of the wake solution was negligible compared to the near-body solution due to the efficient Cartesian mesh topology and a drastic reduction in cell count, solving typically only $\mathcal{O}(10^5)$ cells. All simulations were compared after two full rotor revolutions, after the mean rotor loads converged. Since the flow is stalled over most of the blade at this operating condition, unsteady variations of 8% of the mean thrust and root flap bending were observed. Variations in torque were within 15% of the mean torque value.

The blade pressure distributions for the different interpolation methods are plotted in Fig. 8 at select radial locations along the blade to highlight the effects of applying different interpolation methods. Results at other radial locations were not sensitive to the choice of data transfer method in this case. The greatest variability is observed near to the blade root ($r/R = 0.30$). Increasing interpolation accuracy reduces the overprediction in suction near the leading edge while simultaneously reducing the underprediction in suction closer to the trailing edge. This has the overall effect of improving the accuracy of the pressure distribution compared to experiment. While the integrated pressure difference remains unchanged (i.e., the normal force at $r/R = 0.3$, Fig. 9(a)) these corrections are more strongly reflected in the section pitching moment distribution (Fig. 9(b)). Further outboard at $r/R = 0.63$, the predicted pressure distributions are comparable between all results. The reduction in pressure error is approximately 15% near mid-chord when interpolating with the W2 function. Overall, the sectional pitching moment deviation from experiment measured in terms of root-mean-squared (RMS) error is reduced by 32% and 19% when applying RBF interpolations (Fig. 9b). Improvements are also observed in the section normal force distribution (Fig. 9a) when applying the W2 function, with RMS errors reduced by 14%.

The cost of applying a cloud-based RBF method in parallel computations is compared with trilinear interpolation cost in Table 5 for varying numbers of processors. For small numbers of processors, the workload per processor is relatively high; however, the cost of the interpolation alone account for only 0.5% of the overall cost per iteration, regardless of interpolation method. As the number of parallel processes increases, the solver cost per iteration decreases and the relative cost of the RBF interpolations increases. In all cases, the interpolation cost for the cloud-based methods is less than 1% of the overall cost per iteration.

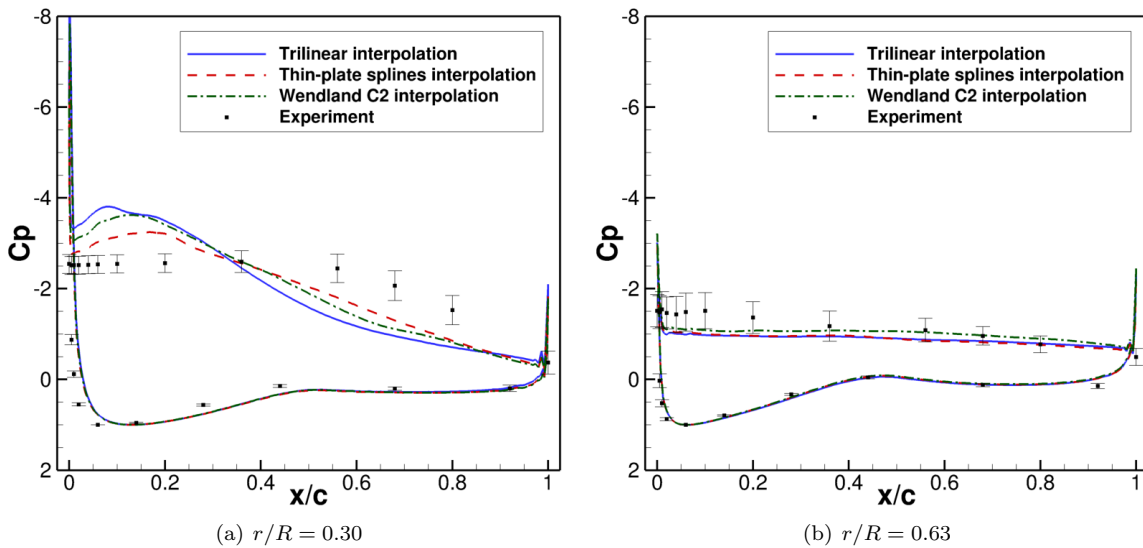


Figure 8. Comparison of pressure coefficients at radial stations corresponding to experimental measurements for a hybrid isolated rotor, calculated with linear and RBF interpolated wake velocities.

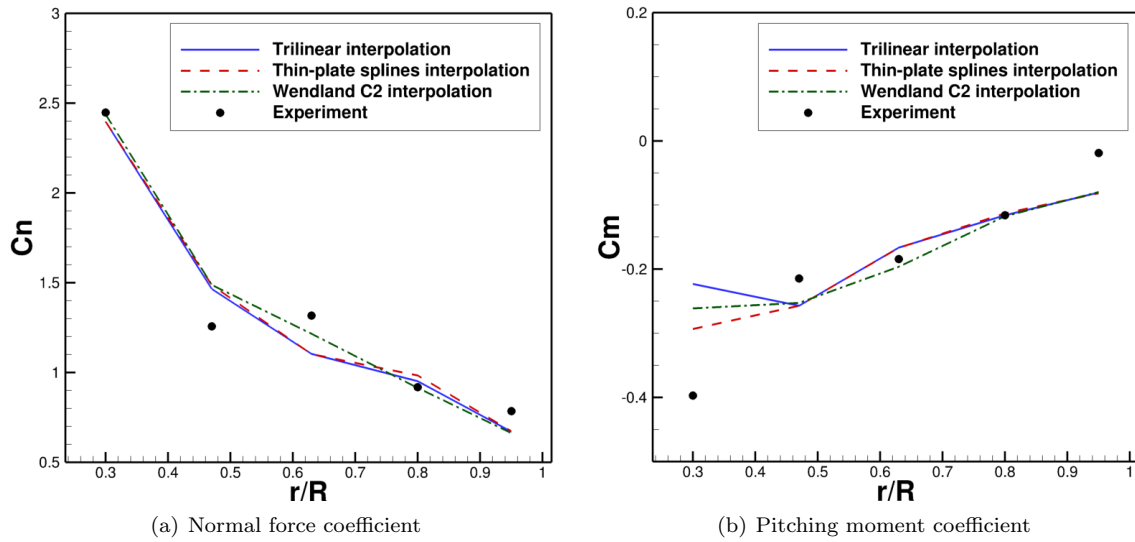


Figure 9. Sectional airloads for hybrid isolated rotor calculations with linear and RBF interpolated wake velocities.

Table 5. Interpolation cost in terms of averaged wallclock time per step for the wind turbine rotor evaluation case.

Hybrid Interface Method	# of processors	Average interpolation cost/step [s]	Fraction of URANS cost/step
Trilinear interpolation	64	1.12	0.50%
	128	0.57	0.48%
	256	0.31	0.44%
Thin-plate spline	64	1.08	0.49%
	128	0.95	0.83%
	256	0.62	0.91%
Wendland C^2	64	1.10	0.48%
	128	0.96	0.80%
	256	0.62	0.88%

V. Conclusions

Cloud-based interpolation methods have been successfully applied to overset URANS and hybrid methodologies on general unstructured grids with minimal interface modifications. The effectiveness of the approach when applying two different radial basis functions verifies the robustness of the algorithm for a variety of flow fields. Specific findings include:

- The value of the cloud-based approach in overset configurations with orphans has been clearly demonstrated. By enabling both interpolation and extrapolation, uncertainty associated with inadequate grid overlap is eliminated. Transient massflow errors are reduced by up to two orders of magnitude for a simple evaluation case of a convecting vortex. For more complex aerodynamics, the accumulation of overset conservation errors may be more significant and the application of an improved data transfer technique can increase solution fidelity without additional spatial or temporal refinement.
- The three-dimensional unsteady, separated flow field in the wake of a ship hangar demonstrated sensitivity to the choice of interpolation method. Even though the overset boundaries were located approximately half a ship length away from the ship, radial basis function overset interpolation was able to reduce errors in the averaged velocity field by up to 35% and improve predictions of flow separation location on the flight deck by 7%. This indicates that for high-resolution computational grids, overset errors may propagate from overset boundaries to distances on the order of the problem reference length.
- For the hybrid rotor simulation, the effect of the improved data transfer between the near-body and the wake is most apparent near the blade root where the shed vorticity persists near the rotor for a long period of time. Up to 32% improvement in pitching moment correlations with experiment with the RBF interpolation method underscores the importance of accurate data transfer.
- For large simulations with node counts of $\mathcal{O}(10^6)$ or larger, the increased interpolation cost was 6% for overset an simulation and less than 1% for a hybrid simulation. The added overset cost may be reduced by optimizing and minimizing the amount of overlap between grids, which reduces the number of data transfers required.

VI. Acknowledgments

The computational work was supported in part by the Office of Naval Research (ONR) under the research grant “High-Accurate Physics-Based Wake Simulation Techniques,” with guidance from technical monitor Dr. Judah Milgram. Computing resources were provided by the Department of Defense High Performance Computing (HPC) Modernization Program.

This paper was prepared as an account of work sponsored by an agency of the United States (U.S.) Government. Neither the U.S. Government nor any agency thereof, nor any of their employees, makes any warranty, express or implied, or assumes any legal liability or responsibility for the accuracy, completeness, or usefulness of any information, apparatus, product, or process disclosed, or represents that its use would not infringe privately owned rights. Reference herein to any specific commercial product, process, or service by trademark, manufacturer, or otherwise does not necessarily constitute or imply its endorsement, recommendation, or favoring by the U.S. Government or any agency thereof. The views and opinion expressed herein do not necessarily state or reflect those of the U.S. Government or any agency thereof.

References

- ¹Steger, J., Dougherty, F., and Benek, J., “A Chimera Grid Scheme,” *American Society of Mechanical Engineers, Fluids Engineering Division*, Vol. 5, 1983, pp. 59–69.
- ²Benek, J., Steger, J., and Dougherty, F., “A Flexible Grid Embedding Technique with Application to the Euler Equations,” *6th AIAA Computational Fluid Dynamics Conference*, No. AIAA-83-1944, Danvers, Massachusetts, July 13–15, 1983.
- ³Abras, J., Lynch, C. E., and Smith, M., “Computational Fluid Dynamics-Computational Structural Dynamics Rotor Coupling Using an Unstructured Reynolds-Averaged Navier-Stokes Methodology,” *Journal of the American Helicopter Society*, Vol. 57, No. 1, Jan 2012, pp. 1–14.
- ⁴Lynch, C. E. and Smith, M. J., “Unstructured Overset Incompressible Computational Fluid Dynamics for Unsteady Wind Turbine Simulations,” *Wind Energy*, Vol. 16, October 2013, pp. 1033–1048.

- ⁵Power, G. D., Gudenkauf, J. A., Masters, J., Calahan, J. A., and Aboulmouna, M., "Integration of USM3D into the Store-Separation Process: Current Status and Future Direction," *47th AIAA Aerospace Sciences Meeting and Exhibit*, AIAA-2009-339, Orlando, Florida, January 5–8, 2009.
- ⁶Noack, R. W., "Resolution Appropriate Overset Grid Assembly for Structured and Unstructured Grids," *16th AIAA Computational Fluid Dynamics Conference*, AIAA-2003-4123, Orlando, Florida, June 23–26, 2003.
- ⁷Sitaraman, J., Floros, M., Wissink, A., and Potsdam, M., "Parallel Domain Connectivity Algorithm for Unsteady Flow," *Journal of Computational Physics*, Vol. 229, No. 12, 2010, pp. 4703–4723.
- ⁸Gaitonde, D. and Visbal, M., "Padé-type Higher-Order Boundary Filters for the Navier-Stokes Equations," *AIAA Journal*, Vol. 38, No. 11, 2000, pp. 2103–2112.
- ⁹Noack, R. W., "DiRTlib: A Library to Add an Overset Capability to Your Flow Solver," *17th AIAA Computational Fluid Dynamics Conference*, No. AIAA-2005-5116, Toronto, Ontario, June 6–9, 2006.
- ¹⁰Rogers, S. E., Roth, K., Nash, S. M., Baker, M. D., Slotnick, J. P., Whitlock, M., and Cao, H. V., "Advances in Overset CFD Processes Applied to Subsonic High-Lift Aircraft," *18th AIAA Applied Aerodynamics Conference*, No. AIAA-2000-4216, Denver, Colorado, August 14–17, 2000.
- ¹¹Platt, S. C., *Parachute Extraction of a Generic Store from a C-130; a CFD Proof of Concept*, Master's thesis, Air Force Institute of Technology, Wright-Patterson Air Force Base, Ohio, March 2005, <http://www.dtic.mil/docs/citations/ADA434226>.
- ¹²Franke, R., "Scattered Data Interpolation: Tests of Some Methods," *Mathematics of Computations*, Vol. 38, No. 157, 1982, pp. 181–200.
- ¹³Smith, M. J., Hodges, D. H., and Cesnik, C. E. S., "An Evaluation of Computational Algorithms to Interface Between CFD and CSD Methodologies," Tech. Rep. WL-TR-96-3055, Air Force Wright Laboratory, November 1995.
- ¹⁴Wendland, H., *Scattered Data Approximation*, Cambridge University Press, New York, NY, 2005.
- ¹⁵Lee, P. K., *CFD/CSD Grid Interfacing of Three-Dimensional Surfaces by Inverse Isoparametric Mapping*, Master's thesis, Massachusetts Institute of Technology, 2001, <http://dspace.mit.edu/handle/1721.1/81568>.
- ¹⁶Quon, E., Smith, M., Whitehouse, G., and Wachspress, D., "Hierarchical Variable Fidelity Methods for Rotorcraft Aerodynamic Design and Analysis," *Proceedings of the 67th American Helicopter Society Annual Forum*, Virginia Beach, Virginia, May 3–5, 2011.
- ¹⁷Wachspress, D. A., Yu, K., Saberi, H., Hasbun, M. J., Ho, J. C., and Yeo, H., "Helicopter Rotor Airload Predictions with a Comprehensive Rotorcraft Analysis," *Proceedings of the 68th American Helicopter Society Annual Forum*, Fort Worth, Texas, May 1–3, 2012.
- ¹⁸Quon, E. W., Smith, M. J., and Whitehouse, G. R., "A Novel Computational Approach to Unsteady Aerodynamic and Aeroelastic Flow Simulation," *International Forum on Aeroelasticity & Structural Dynamics*, Royal Aeronautical Society, Bristol, United Kingdom, June 24–26 2013.
- ¹⁹Buhmann, M., "A New Class of Radial Basis Functions with Compact Support," *Mathematics of Computation*, Vol. 70, No. 233, 2000, pp. 307–318.
- ²⁰Smith, M. J., Hodges, D. H., and Cesnik, C. E. S., "An Evaluation of Computational Algorithms Suitable for Fluid-Structure Interaction," *AIAA Journal of Aircraft*, Vol. 37, No. 2, 2000, pp. 282–294.
- ²¹de Boer, A., van Zuijlen, A. H., and Bijl, H., *Advanced Computational Methods in Science and Engineering*, chap. Radial Basis Functions for Interface Interpolation and Mesh Deformation, 2010, pp. 143–178.
- ²²Rendall, T. and Allen, C., "Efficient Mesh Motion Using Radial Basis Function with Data Reduction Algorithms," *Journal of Computational Physics*, Vol. 228, No. 17, 2009, pp. 6231–2649.
- ²³Costin, W. and Allen, C., "Numerical Study of Radial Basis Function Interpolation for Data Transfer Across Discontinuous Mesh Interfaces," *International Journal for Numerical Methods in Fluids*, Vol. 72, 2013, pp. 1076–1095.
- ²⁴Rendall, T. and Allen, C., "Evaluation of Radial Basis Functions for CFD Volume Data Interpolation," *48th AIAA Aerospace Sciences Meeting and Exhibit*, No. AIAA-2010-1414, Orlando, Florida, January 4–7, 2010.
- ²⁵Schaback, R., "Creating Surfaces from Scattered Data Using Radial Basis Functions," *Mathematical Methods for Curves and Surfaces*, 1995, pp. 477–496.
- ²⁶Beckert, A. and Wendland, H., "Multivariate Interpolation for Fluid-Structure-Interaction Problems Using Radial Basis Functions," *Aerospace Science and Technology*, Vol. 5, No. 2, 2001, pp. 125–134.
- ²⁷Wendland, H., *Topics in Multivariate Approximation and Interpolation*, chap. Computational Aspects of Radial Basis Function Approximation, Elsevier, 2005, pp. 231–256.
- ²⁸Quon, E. W., *Data Transfer Strategies for Overset and Hybrid Computational Methods*, Ph.D. thesis, Georgia Institute of Technology, Atlanta, Georgia, 2014.
- ²⁹Anderson, W. K. and Bonhaus, D. L., "An Implicit Upwind Algorithm for Computing Turbulent Flows on Unstructured Grids," *Computers & Fluids*, Vol. 23, No. 1, 1994, pp. 1–21.
- ³⁰Biedron, R., Vatsa, V., and Atkins, H., "Simulation of Unsteady Flows Using an Unstructured Navier-Stokes Solver on Moving and Stationary Grids," *23rd AIAA Applied Aerodynamics Conference*, No. AIAA-2005-5093, Toronto, Ontario, June 6–8, 2005.
- ³¹Noack, R. W., Boger, D. A., Kunz, R. F., and Carrica, P. M., "Suggar++: An Improved General Overset Grid Assembly Capability," *AIAA 19th Computational Fluid Dynamics Conference*, No. AIAA-2009-3992, Austin, Texas, June 22–25, 2009.
- ³²Whitehouse, G., Boschitsch, A., Quackenbush, T., Wachspress, D., and Brown, R. E., "Novel Eulerian Vorticity Transport Wake Module for Rotorcraft Flow Analysis," *Proceedings of the 63rd American Helicopter Society Annual Forum*, Virginia Beach, Virginia, May 1–3, 2007.
- ³³Whitehouse, G. R. and Tadghighi, H., "Investigation of Hybrid Grid-Based Computational Fluid Dynamics Methods for Rotorcraft Flow Analysis," *Journal of the American Helicopter Society*, Vol. 56, No. 032004, 2011, pp. 1–10.

³⁴Whitehouse, G. R. and Boschitsch, A. H., "Toward the Next Generation of Grid-Based Vorticity-Velocity Solvers for General Rotorcraft Flow Analysis," *Proceedings of the 69th American Helicopter Society Annual Forum*, Phoenix, Arizona, May 21–23, 2013.

³⁵Visbal, M. R. and Gaitonde, D. V., "High-Order-Accurate Methods for Complex Unsteady Subsonic Flows," *AIAA Journal*, Vol. 37, No. 10, 1999, pp. 1231–1239.

³⁶Press, W., Flannery, B., Teukolsky, S., and Vetterling, W., *Numerical Recipes in FORTRAN: The Art of Scientific Computing*, chap. 2, Cambridge University Press, New York, NY, 2nd ed., 1992.

³⁷Roper, D., Owen, I., Padfield, G., and Hodge, S., "Integrating CFD and Piloted Simulation to Quantify Ship-Helicopter Operating Limits," *The Aeronautical Journal*, Vol. 110, No. 1109, 2006, pp. 419–428.

³⁸Wilkinson, C., Zan, S., Gilbert, N., and Funk, J., "Modelling and Simulation of Ship Air Wakes for Helicopter Operations—A Collaborative Venture," *RTO AVT Symposium on "Fluid Dynamics Problems of Vehicles Operating near or in the Air-Sea Interface"*, Amsterdam, The Netherlands, 1998.

³⁹Quon, E., Smith, M. J., Rosenfield, N., and Whitehouse, G., "Investigation of Ship Airwakes Using a Hybrid Computational Methodology," *Proceedings of the 70th American Helicopter Society Forum*, Montreal, Canada, May 20–22, 2014.

⁴⁰Wakefield, N., Newman, S., and Wilson, P., "Helicopter Flight Around a Ship's Superstructure," *Institution of Mechanical Engineers Part G: Journal of Aerospace Engineering*, Vol. 216, 2002, pp. 13–28.

⁴¹Nadge, P. M. and Govardhan, R., "High Reynolds Number Flow Over a Backward-Facing Step: Structure of the Mean Separation Bubble," *Experiments in Fluids*, Vol. 55, No. 1, January 2014, pp. 1–22.

⁴²Thresher, R., Robinson, M., and Veers, P., "The Future of Wind Energy Technology in the United States," Tech. Rep. NREL/CP-500-43412, National Renewable Energy Laboratory, October 2008.

⁴³Herbert, G. J., Iniyar, S., Sreevalsan, E., and Rajapandian, S., "A Review of Wind Energy Technologies," *Renewable and Sustainable Energy Reviews*, Vol. 11, No. 6, August 2007, pp. 1117–1145.

⁴⁴Quon, E. W. and Smith, M. J., "Advanced Methods for Predicting Three-Dimensional Unsteady Flows Around Wind Turbines," *The Aeronautical Journal*, Submitted September 18, 2014 (see also Ref. 28).

⁴⁵Hand, M., Simms, D., Fingersh, L., Jager, D., Cotrell, J., Schreck, S., and Larwood, S., "Unsteady Aerodynamics Experiment Phase VI: Wind Tunnel Test Configurations and Available Data Campaigns," Tech. Rep. TP-500-29955, National Renewable Energy Laboratory, December 2001.